

De novo structural ensemble determination from single-molecule X-ray scattering: A Bayesian approach

Steffen Schultze¹, Helmut Grubmüller^{2*}

Max Planck Institute for Multidisciplinary Sciences

¹sschult@mpinat.mpg.de ²hgrubmu@gwdg.de

April 17, 2023

Abstract

Single molecule X-ray scattering experiments with free electron lasers have opened a new route to the structure determination of biomolecules. Because typically only very few photons per scattering image are recorded and thus the signal-to-noise ratio is very low in this extreme Poisson regime, structure refinement is quite challenging. In addition, in each scattering event the orientation of the biomolecule is random and unknown. As a further layer of complexity, many biomolecules show structural heterogeneity and conformational transitions between different distinct structures; these structural dynamics are averaged out by existing refinement methods. To overcome these limitations, here we developed and tested a rigorous Bayesian approach and demonstrate that it should be possible to determine not only a single structure, but an entire structural ensemble from these experiments. Using 10^6 synthetic scattering images generated from molecular dynamics trajectories, our approach was able to resolve ensembles of eight alanine dipeptide conformers at 2 Å resolution; similarly, we determined the unfolded ensemble of the protein chignolin at 4 – 7 Å resolution using $1.2 \cdot 10^7$ images. Unexpectedly, much fewer images are required to determine an ensemble of n structures of m atoms each than a single structure of $n \times m$ atoms, i.e., of the same total number of degrees of freedom. These findings show that X-ray scattering experiments using state-of-the-art free electron lasers should allow one to determine not only biomolecular structures, but whole structure ensembles and, ultimately, ‘molecular movies’.

1 Introduction

Ultrashort pulse X-ray scattering experiments offer the possibility to take ‘snapshots’ of biomolecular structures with atomistic spatial and femtoseconds time resolution [1–4]. Still, most current experiments focus on nano-crystals [5–12]. Like classical X-ray crystallography, these average over many molecules and, therefore, time resolved structure determination requires strict synchronization, typically by optical laser pulses [12]. Scattering on single particles or molecules avoids this limitation and should enable us to advance towards structure ensembles and, ultimately, time resolved conformational and functional motions without the need for synchronization [13, 14].

In such ‘hit and destroy’ experiments, a stream of single molecules is exposed to a beam of high intensity femtosecond X-ray free electron laser (XFEL) pulses (Fig. 1a). For each hit the positions of the scattered photons (red dots) on the detector are recorded as a scattering image [15]. Importantly, the ultra-short pulses serve to outrun the subsequent destruction of the particles due to radiation damage, but also imply that only very few photons are being recorded for each molecule [3].

The feasibility of this approach has already been demonstrated by a number of experiments [16–18], but so far only structures of relatively large specimen at low resolution have been successfully determined, for instance of entire mimivirus particles [16, 17] (450 nm in diameter) and coliphage viruses [18] (20 nm in diameter). Whereas for large specimens many photons are scattered per image, for example 10^7 for the mimivirus [16, 17], for typical proteins only 10-100 coherently scattered photons per image are expected [19, 20], which further complicates structure determination particularly for small molecules. Such images can be obtained with an intensity of 10^{12} photons per pulse at 5 keV and a 1 μm beam diameter [21], for example from the XFELs at DESY or SLAC.

Most importantly, the orientation of the molecules at the time of scattering is typically unknown, which poses an additional and substantial refinement challenge. These issues are particularly challenging for the structure refinement of small specimen such as proteins or protein complexes at near-atomic resolution. A number of methods have been proposed to address these issues, such as orientation determination methods [22–30] and manifold embedding algorithms [31–34], which, however, typically require 100 to 1000 photons per scattering image. As an alternative, correlation based approaches [35–39] have recently allowed substantial advancements and have been shown to require, quite counterintuitively, only three photons per image [21]. However, as for all other approaches proposed so far, it is impossible to systematically include shot noise, incoherently scattered photons, background scattering, or detector noise in the structure refinement.

Finally, many biomolecules show structural heterogeneity and conformational dynamics between different distinct structures, which, when resolved, would provide a direct view on biomolecular function. Hence, and similar to the current main challenge in cryogenic electron microscopy [40], not one but many structures need to be extracted from the scattering images. In this scenario, in addition to the orientation, also the current conformer for each scattering image is unknown. Whereas both orientation determination methods and manifold-based methods have been applied to determine multiple conformational structures [41, 42], the required large number of photons per image precludes their application to single biomolecules.

To overcome these issues, we developed and assessed a rigorous Bayesian method for multiple structure determination from single-molecule scattering images. We will demonstrate that this method can not only determine a single structure, but also ensembles consisting of multiple structures

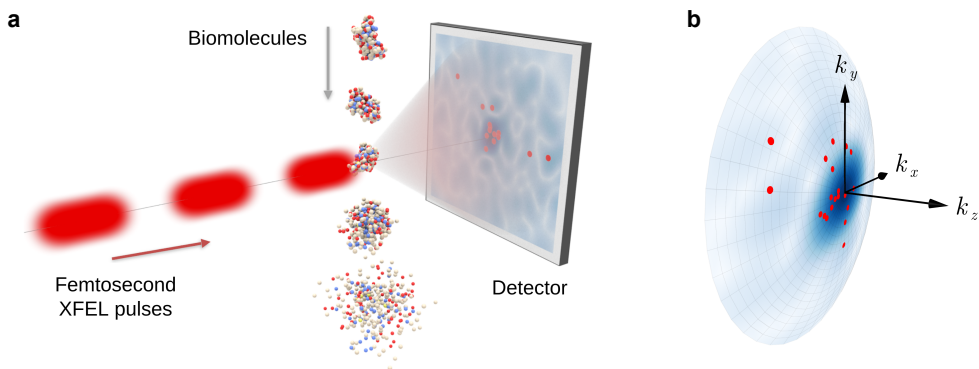


Figure 1: Single molecule scattering experiment. **a** A stream of single molecules is hit by femtosecond X-ray pulses, and the scattered photons are recorded as images (image reproduced from von Ardenne et al. [21]). **b** The scattered photons (red dots) are distributed on the Ewald sphere according to the 3D-intensity function I (blue).

at high resolution. Unexpectedly, much fewer images are required for refining an ensemble of n conformers consisting of m atoms each than for refining a single structure consisting of $m \times n$ atoms, which should render biomolecular ensemble determination accessible to state-of-the-art experiments.

2 Results

Summary of the approach. For each scattering image, the positions of the recorded photons specify vectors $\mathbf{k}_1, \dots, \mathbf{k}_l$ on the Ewald sphere in Fourier space (red dots in Fig. 1b). The probability of observing a photon at a particular position on the detector is proportional to the 3D intensity function $I(\mathbf{k}) \propto |\mathcal{F}\{\mathbf{R}\rho_i\}(\mathbf{k})|^2$ at the corresponding position \mathbf{k} on the Ewald sphere, which in turn is given by the Fourier transform of the electron density ρ_i of conformer i . Here, \mathbf{R} is the unknown orientation of the molecule for this particular image.

It follows that the probability of observing an image with photon positions $\mathbf{k}_1, \dots, \mathbf{k}_l$ is obtained by averaging over both the conformational ensemble $\boldsymbol{\rho} = \{\rho_1, \dots, \rho_n\}$ with weights $\mathbf{w} = \{w_1, \dots, w_n\}$ as well as over all orientations \mathbf{R} . Because the scattering images are statistically independent from each other, the total probability of observing the complete set of all images \mathcal{I} reads

$$P(\mathcal{I} | \boldsymbol{\rho}, \mathbf{w}) \propto \prod_{(\mathbf{k}_1, \dots, \mathbf{k}_l) \in \mathcal{I}} \sum_{i=1}^n w_i \int_{\text{SO}(3)} P(\mathbf{k}_1, \dots, \mathbf{k}_l | \mathbf{R}\rho_i) d\mathbf{R}. \quad (1)$$

This probability serves to determine either a single structure or a structural ensemble by sampling from the Bayesian posterior probability $P(\boldsymbol{\rho}, \mathbf{w} | \mathcal{I}) \propto P(\mathcal{I} | \boldsymbol{\rho}, \mathbf{w})P(\boldsymbol{\rho}, \mathbf{w})$ using a Markov chain Monte Carlo approach. For the prior $P(\boldsymbol{\rho}, \mathbf{w})$ the orientations are assumed to be uniformly distributed. To minimize the number of required degrees of freedom, and as a means of regularization, we chose a physically motivated representation of each ρ_i in terms of a sum of Gaussian functions, which also completes the definition of the prior.

For a typical protein consisting of 50 to several hundred residues, the number of required degrees of freedom remains large and poses a formidable sampling challenge. To address this issue, we have implemented a hierarchical simulated annealing approach. Starting at very low resolution, the

macromolecular structures were sampled in multiple hierarchical stages of increasing resolution. To increase the sampling efficiency, in each of these stages, for each Markov step the previous ensemble of structures of maximal posterior probability was used as a proposal density. To this end, the scattering images that would have been observed for a smoothed low resolution copy of the original molecule were obtained from the original images by rejection sampling using the convolution theorem (see the Methods section).

Further, we adapted the Bayesian formalism such that only those images are used which contain new information, that is, photons for which the magnitude of \mathbf{k} is larger than the threshold of the resolution from the previous stage. With increasing resolution, the fraction of such useful images becomes very small, thus enhancing computational efficiency up to two orders of magnitude. The approach is described in detail in the Supplementary Information.

Sample test refinements. Because our Bayesian approach uses all available information, we expect it to require fewer scattering images to achieve a certain resolution than, for example, correlation based methods. To assess this aspect, we first tested our method on the single structure level, using the same 46-residue protein crambin [43] as in our previous study [21]. A total of 10^8 noise-free synthetic images were generated, containing a realistic average of 15 photons each. From these, the structure was solved in five hierarchical stages (Fig. 2a), increasing the number of degrees of freedom by a factor of two in each stage. For the final stage, a representation of ρ consisting of 184 Gaussian functions was used, which is four times the number of residues. For more details see Supplementary Note 1. Indeed, using only half of the total number of scattered photons, a similar Fourier shell correlation resolution [44] of 4.2 Å (Fig. 2b) is obtained as with the previous correlation based method [21].

Next, to demonstrate that our method can resolve not only a single protein structure, but also ensembles of multiple conformers, we used three molecular dynamics trajectories of alanine dipeptide [45] of length 250 ns each to generate 10^6 scattering images, using a randomly chosen snapshot for each image. As before, an average of 15 photons per image were generated. Using our approach, a weighted ensemble of eight conformers was determined from these images (Fig. 3), with each conformer being described by a sum of 10 Gaussian functions. To obtain sufficient statistics, a total of 10 independent simulated annealing runs were carried out, using the same image set.

To assess the quality of the obtained structure ensemble, for each of the eight structures the resolution with respect to its nearest neighbor in the input trajectories was calculated using Fourier shell correlations [44] (Fig. 3b), resulting in a weighted average resolution of 1.8 Å. This result shows that the obtained eight structures are indeed close to the reference ensemble. To also assess the accuracy of the entire ensemble, for each time step in the input trajectories, the resolution with respect to its nearest neighbor among all the determined structures was calculated (Fig. 3d). As a main result we found that 90% of the input trajectories are within 2.1 Å Fourier shell correlation resolution of the determined structures, and that all of the trajectory frames are within 2.5 Å resolution of the determined structures, thus demonstrating atomistic resolution. Figure 3e compares the 10 obtained ensembles with the reference ensemble using a Ramachandran plot [46] showing the distribution of the torsion angles ϕ and ψ . For each of the determined structures its nearest neighbor in the input trajectories was used to compute these angles. As can be seen, the reference density is well represented by the determined structures.

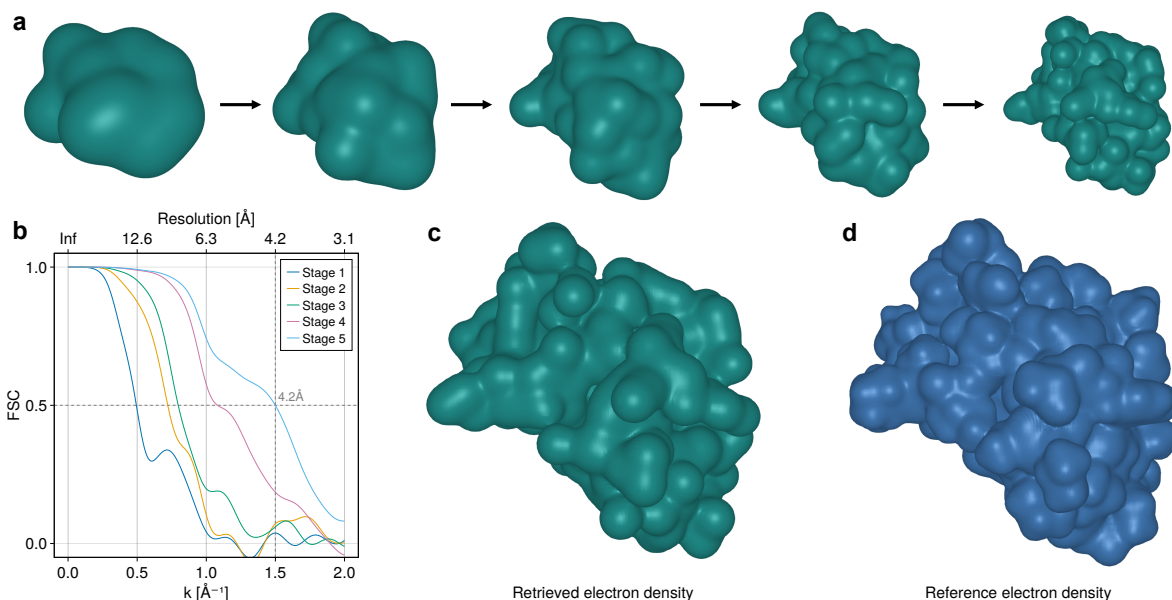


Figure 2: Structure determination of Crambin. **a** Hierarchical stages of retrieved electron densities. **b** Fourier shell correlation between the retrieved densities and the reference density. **c** Retrieved electron density. **d** Reference electron density.

Next, we asked if our method is also capable of extracting structural ensembles for the larger mini-protein chignolin [47], comprising 10 residues. To that end, 50 molecular dynamics trajectories of length $10 \mu\text{s}$ were used to generate $1.2 \cdot 10^7$ images with, on average, 15 photons each. As a further challenge, this ensemble also contained unfolded structures. From the obtained images, we determined multiple stages of weighted structural ensembles of increasing resolution and increasing number of conformers (Fig. 4a). As above, resolutions were computed using Fourier shell correlations (Fig. 4b,c), finding a weighted average resolution of 4.7 \AA for the folded conformers, and 6.4 \AA for the unfolded conformers. Interestingly, in the final stage one of the six determined weights is nearly zero, suggesting that five conformers suffice for the used number of images at this resolution level. It is also worth noting that the 9% fraction of unfolded states in the reference structure ensemble was correctly identified.

Scaling. For both of the above sample applications described above we observed, unexpectedly, that resolving n conformational structures consisting of m residues each required much fewer scattering images and photons than resolving a single $n \times m$ residue structure of the same total size and complexity — even in cases where the conformers of the ensemble are very different from each other. To investigate this counterintuitive result in more detail, small ‘structures’ consisting of randomly placed Gaussian functions were used. For each combination of parameters, eight independent structure determination runs were performed, and for each run the achieved resolution was determined. The structure weights w_i were chosen to be uniform and kept fixed during the simulated annealing runs.

Figure 5c and 5f show for each combination of parameters the smallest number of images for which all of the replicas achieved a resolution better than a given threshold. As can be seen in Fig. 5c, for

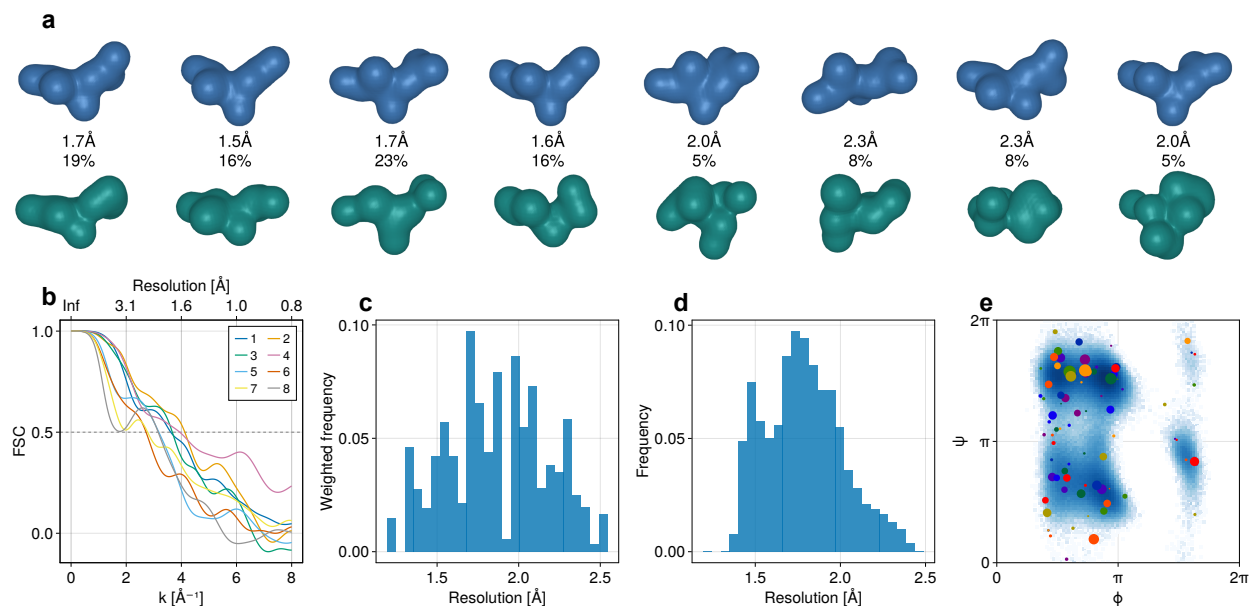


Figure 3: Structural ensemble determination of the alanine dipeptide. **a** Reconstructed conformers (green), the corresponding weights, and the nearest neighbors in the input trajectories (blue) with the corresponding resolutions. **b** Fourier shell correlations used to compute these resolutions (from left to right). **c** Weighted resolution distribution for 10 independent runs from the the same data. **d** Resolution distribution over the time steps of the input trajectories relative to their nearest neighbors among the determined structures from all 10 runs. **e** Ramachandran plot for the input trajectories (shown as a density) and the determined structures from all 10 runs (points, the colors indicate the separate runs).

the structure ensemble of n conformations with m residues each, the required number of images is approximately proportional to n^2 , the square of the number of conformations. This finding is in line with a theoretical argument showing that the information content of a single image is in this case proportional to $1/n^2$ (Supplementary Note 2). In contrast, the number of images required to resolve a single structure of $n \times m$ residues grows even much faster, approaching a power law m^c with an exponent $c \approx 5$ for increasing resolution (Fig. 5f). Hence, for given complexity, ensemble refinement seems to be easier than single structure determination.

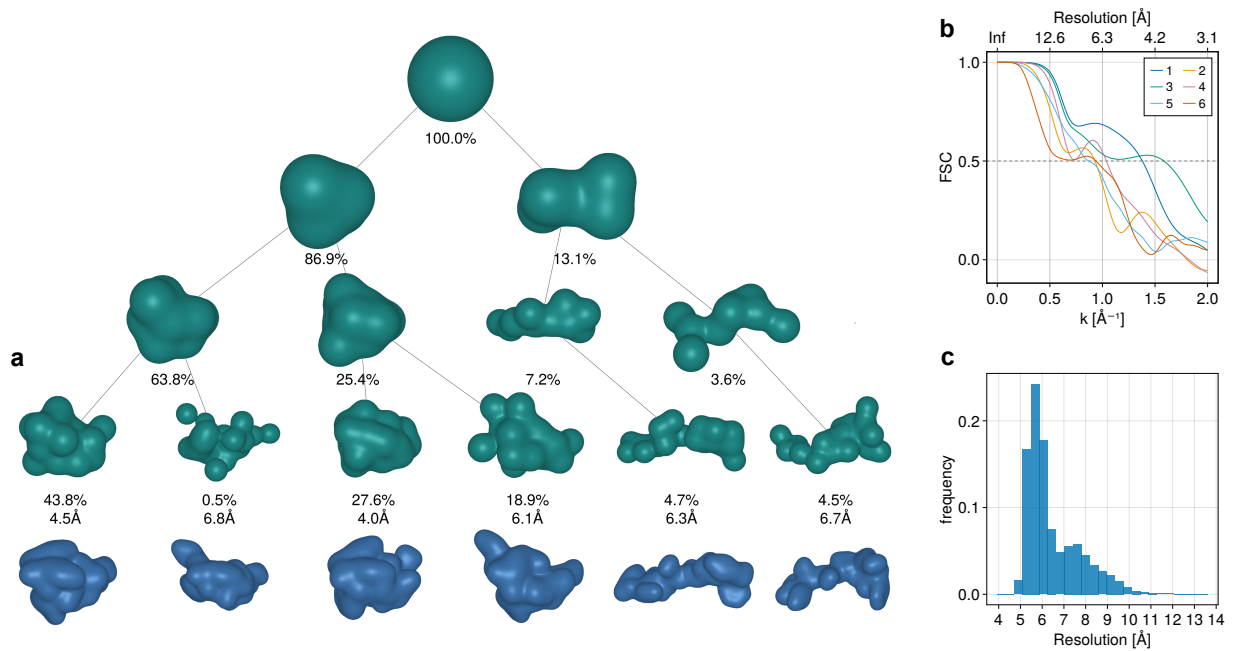


Figure 4: Structural ensemble determination for chignolin. **a** Hierarchical stages of retrieved structures (green) and their nearest neighbors (blue) in the input trajectories with the corresponding resolutions. **b** Fourier shell correlations of the reconstructed structures relative to their nearest neighbors (from left to right). **c** Resolution distribution over the time steps of the input trajectories relative to their nearest neighbors among the determined structures.

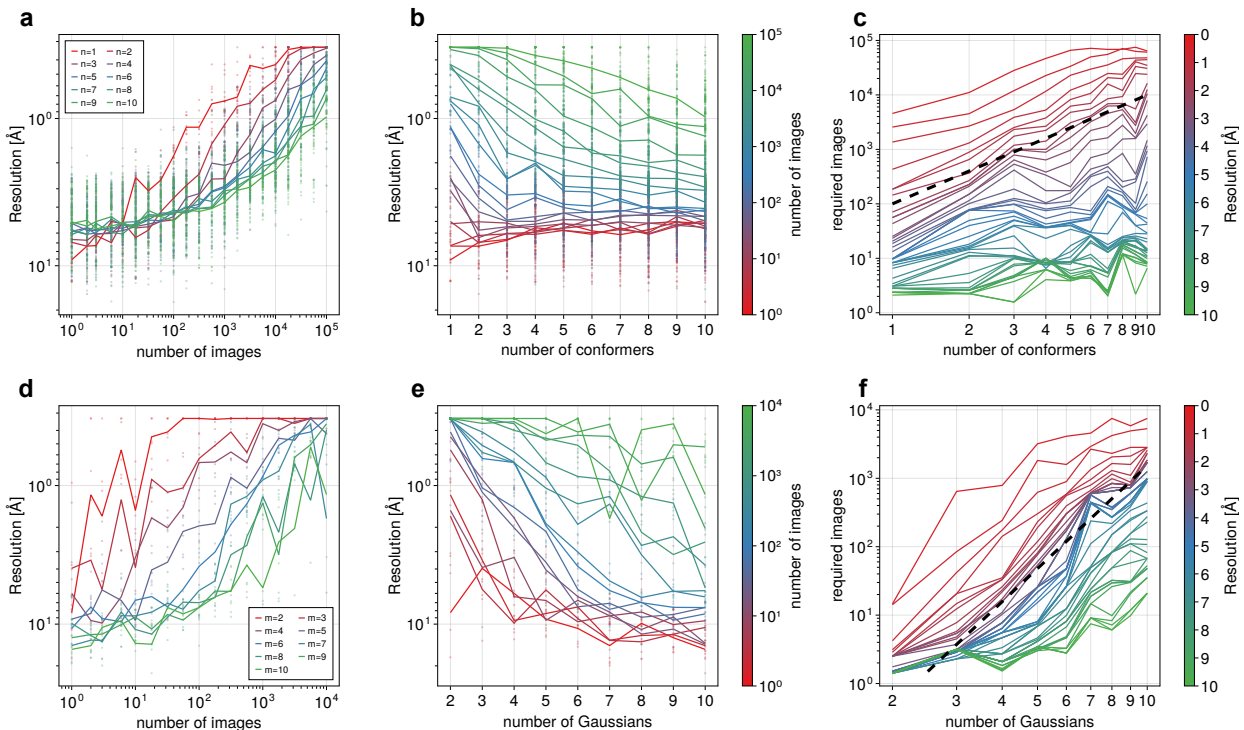


Figure 5: Dependence of the resolution on the number of images, the number of conformations, and the size of the structure. **a** Resolution as a function of the number of images for various numbers of conformations n . **b** Resolution as a function of the number of conformations for various numbers of images. **c** Required number of images to achieve various resolutions as a function of the number of conformations. For comparison, a quadratic relationship is shown (dashed line). **d** Resolution as a function of the number of images for various structure sizes (parameterized by the number of Gaussians m). **e** Resolution as a function of the number of Gaussians for various numbers of images. **f** Required number of images to achieve various resolutions as a function of the number of Gaussians. For comparison, a power law m^5 is shown (dashed line).

3 Discussion

Here we have developed a rigorous Bayesian method for determining biomolecular structures from single molecule X-ray scattering images in the extreme few photon Poisson regime. Using synthetic scattering images generated from simulated X-ray scattering experiments, we have demonstrated that both single structures as well as structural ensembles of small biomolecules can be resolved to near atomic resolution.

Our results for the globular protein crambin show that a similar resolution of 4.2 Å is obtained compared to previous correlation based methods [21] which also require very few photons per scattering image. Because such correlation based methods disregard higher correlations, whereas the full information content of each image is used in our Bayesian approach, the latter should require fewer images. This was indeed observed for the above protein, for which the number of images required to obtain near atomistic resolution was reduced from roughly $2 \cdot 10^8$ to $1 \cdot 10^8$. Assuming a pulse rate of 27,000 per second [48] and a 10% hit fraction, this would reduce required beam time from 20 to 10 hours.

Because the rather small test proteins studied here scatter very few photons, they are conceptually more challenging than larger proteins [24]. For the latter, in contrast, the main bottleneck is computational cost, which will need to be addressed by improved optimization or sampling methods or by utilizing prior structural information, either from structure databases, from AlphaFold [49], or guided by molecular dynamics force fields.

For alanine dipeptide the full conformational ensemble generated by an atomistic simulation was extracted at atomistic resolution of on average 1.8 Å from simulated scattering experiments, in which not only the current orientation of the biomolecule but also its current conformer was unknown. For the 10 amino acid protein chignolin [47] both the folded and unfolded ensembles were resolved, albeit so far at lower resolution. Notably, also the weights corresponding to the folded and unfolded conformers were accurately recovered. Using weighted ensembles allows the number of conformers to be determined dynamically, as demonstrated by vanishing weights for incorrect structure poses.

Unexpectedly few images were required to resolve structural ensembles. Because an ensemble of n conformers consisting of m atoms each has the same number of degrees of freedom as a single structure of $n \times m$ atoms, a similar number of images should be required. However, closer analysis suggests that roughly $O(m^5)$ images are required to resolve a single structure with m atoms. One might therefore expect that $O(n^5 m^5)$ images are required for an ensemble of n such structures. However, our test refinements suggest that only $O(n^2 m^5)$ images are required, consistent with an expected information content of $O(1/n^2)$ for single scattering image. This result suggests that in terms of the required number of scattering images, even determining more complex conformational ensembles should be possible with current experimental technology.

Our Bayesian analysis of structural heterogeneity is similar in spirit to approaches that were successfully applied in cryo-electron microscopy [50–57], which, from a mathematical standpoint, shares some similarities with single molecule X-ray scattering, albeit at a much lower noise level. From a more general perspective, our Bayesian approach represents a systematic and rigorous approach to include shot noise in the extreme Poisson regime characteristic for single molecule X-ray scattering experiments. In contrast to other proposed methods, this Bayesian framework will also allow to include other sources of noise and uncertainty in a conceptually straightforward

manner, such as incoherently scattered photons, background scattering, detector noise, or scattering by disordered water at the biomolecular surface. Proper inclusion of these experimental uncertainties in terms of calibrated forward noise models (e.g., as documented in Ref. [19]) will be the next crucial step towards atomistically resolved multiple structure ensembles. If successful, and in contrast to diffraction experiments on nano-crystals, this single molecule approach might ultimately provide a route to time resolved structures — molecular movies — without the need for synchronization through optical laser pulses.

4 Methods

Structure and structure ensemble representation. Electron density functions of the reference structures or conformers were described by a sum of m of Gaussian functions with atomic positions \mathbf{y}_i , heights h_i and standard deviations σ_i ,

$$\rho(\mathbf{r}) = \sum_{i=1}^m \frac{h_i}{(\sigma_i \sqrt{2\pi})^3} \exp\left(-\frac{1}{2\sigma_i^2} \|\mathbf{r} - \mathbf{y}_i\|^2\right). \quad (2)$$

Electron density functions of the determined structures were described similarly, with one common height $h = h_i$ and one common standard deviation $\sigma = \sigma_i$, which is treated as an unknown and determined together with the positions \mathbf{y}_i . Structural ensembles were represented by a weighted sum of conformers $\boldsymbol{\rho} = \{\rho_1, \dots, \rho_n\}$ with weights $\mathbf{w} = \{w_1, \dots, w_n\}$.

Synthetic data generation. For each of the synthetic scattering images, the photon positions on the detector D were drawn from a probability distribution proportional to the intensity function $I(\mathbf{k}) = |F\{\rho\}(\mathbf{k})|^2$ restricted to the appropriate Ewald sphere. Specifically, generation of each image involved the following steps:

1. A conformation of the molecule is selected randomly from the reference ensemble (for example, consisting of molecular dynamics trajectories),
2. a random orientation \mathbf{R} of the molecule is drawn uniformly from the rotation group $\text{SO}(3)$,
3. the number of scattered photons is drawn from a Poisson distribution with mean $N \int_D I(\mathbf{R}\mathbf{k}) d\mathbf{k}$, where N is the incoming beam intensity,
4. the position of each scattered photon is drawn from the probability distribution proportional to $(I \circ \mathbf{R})|_D$.

The last two steps were implemented using rejection sampling. To this end, a von Mises-Fisher distribution p on D was chosen with high enough standard deviation that $I(\mathbf{k}) \leq p(\mathbf{k})$ everywhere. Then, for each photon, its position \mathbf{k} was drawn from p and it was accepted with probability $I(\mathbf{R}\mathbf{k})/p(\mathbf{R}\mathbf{k})$. The beam intensity N was chosen together with a normalization of ρ such that this procedure accurately produces a Poisson distribution of the desired expected number of photons per image.

Computation of likelihoods. The probability density of observing an image defined by photon positions $\mathbf{k}_1, \dots, \mathbf{k}_l$ given an electron density function ρ with its corresponding intensity function $I(\mathbf{k})$ was computed by averaging over all possible orientations $\mathbf{R} \in \text{SO}(3)$ of the molecule,

$$P(\mathbf{k}_1, \dots, \mathbf{k}_l | \rho) = \frac{N^l}{l!} \int_{\text{SO}(3)} \exp\left(-N \int_D I(\mathbf{R}\mathbf{k}) d\mathbf{k}\right) \left(\prod_{i=1}^l I(\mathbf{R}\mathbf{k}_i)\right) d\mathbf{R}, \quad (3)$$

where for each orientation, the probability is a product of the Poisson distribution for the number of photons l in the image and a factor depending on the photon positions. These integrals were approximated by averaging over a discrete set of typically $r \approx 10^3$ to $r \approx 10^5$ rotations \mathbf{R}_i with weights s_i ,

$$P(\mathbf{k}_1, \dots, \mathbf{k}_l | \rho) \approx \frac{N^l}{l!} \sum_{i=1}^r s_i \exp\left(-N \int_D I(\mathbf{R}_i \mathbf{k}) d\mathbf{k}\right) \prod_{j=1}^l I(\mathbf{R}_i \mathbf{k}_j). \quad (4)$$

The rotations \mathbf{R}_i and their weights s_i are constructed by combining a Lebedev quadrature rule on S^2 with a uniform quadrature rule on S^1 via the Hopf map [58, 59] (Supplementary Note 3).

Simulated annealing and hierarchical sampling. A Monte Carlo simulated annealing approach with the energy function $-\log P$ was used to sample from or maximize the Bayesian posterior probability, as described in detail in the Supplement. To enhance convergence, Bayesian sampling and maximization were performed in multiple hierarchical resolution stages. Starting from a low resolution representation of ρ with correspondingly few degrees of freedom, the number of Gaussian functions was doubled in each stage and the reduced resolution structure determined by the previous stage was used as a proposal density (see Supplement). To calculate likelihoods for the reduced resolution structures, lower resolution scattering images were generated from the original images by rejection sampling, that is, by removing each photon in the original images with probability $1 - \exp(-\sigma^2 k^2/2)$. By construction, this rejection scheme samples from a Fourier transformed density $I_\rho \cdot \exp(-\sigma^2 |\mathbf{k}|^2/2)$ which, by the convolution theorem, corresponds to a smoothed real space density $\tilde{\rho} = \rho * \mathcal{N}(\sigma)$ obtained as the convolution of ρ with a Gaussian kernel with width (resolution) σ . Computational efficiency was further increased substantially by selecting only those original images for the likelihood computations that actually contain useful information at the respective resolution. As described in the Supplement, the Bayesian formalism allows for removing this selection bias.

Structure alignment and resolution estimate. Because the orientations of the obtained structures are irrelevant, these were rotationally aligned to each other by minimizing the cost function

$$d(\mathbf{S}) = \frac{1}{n} \sum_{i=1}^n \min_{j=1}^m \|\mathbf{y}_i - \mathbf{S}\mathbf{y}'_j\| + \frac{1}{m} \sum_{j=1}^m \min_{i=1}^n \|\mathbf{y}_i - \mathbf{S}\mathbf{y}'_j\|. \quad (5)$$

Here, the positions $\mathbf{y}_1, \dots, \mathbf{y}_n$ and $\mathbf{y}'_1, \dots, \mathbf{y}'_m$ define two structures per equation (2) and \mathbf{S} is a rotation matrix $\mathbf{S} \in \text{O}(3)$. Both rotations and reflections were included, as X-ray scattering images do not distinguish between mirror images.

The resolution of the aligned structures was estimated using Fourier shell correlations [44],

$$\text{FSC}(k) = \frac{\int_{\|\mathbf{k}\|=k} \hat{\rho}_1(\mathbf{k})^* \hat{\rho}_2(\mathbf{k}) d\mathbf{k}}{\sqrt{\int_{\|\mathbf{k}\|=k} |\hat{\rho}_1(\mathbf{k})|^2 d\mathbf{k}} \sqrt{\int_{\|\mathbf{k}\|=k} |\hat{\rho}_2(\mathbf{k})|^2 d\mathbf{k}}}, \quad (6)$$

where ρ_1 are ρ_2 the structures to be compared and $\hat{\rho}$ denotes the Fourier transform of ρ . Accordingly, the achieved resolution was determined as $2\pi/k_{\text{fsc}}$, where k_{fsc} is the threshold at which the Fourier shell correlation drops below 1/2, providing a conservative estimate [44].

Molecular dynamics simulations. All atomistic simulation trajectories were generated using the GROMACS 2018 software package [60] with the Charmm36mm force field [61] and the OPC water model [62]. For chignolin, the starting structure was taken from the Protein Data Bank [63], entry 5AWL [47]. All hydrogen atoms were described by virtual sites [64]. Each protein was placed within a triclinic water box, such that the smallest distance between protein surface and box boundary was larger than 1.5 nm. Sodium and chloride ions were added to neutralize the system, corresponding to a physiological concentration of 150 mmol/l. Energy minimization was performed using steepest descent for $5 \cdot 10^4$ steps. Each system was subsequently equilibrated for 0.5 ns in the *NVT* ensemble, and subsequently for 1.0 ns in the *NPT* ensemble at 1 atm pressure and temperature 300 K using an integration time step of 2 fs. The velocity rescaling thermostat [65] and Parrinello-Rahman pressure coupling [66] were used with coupling coefficients of $\tau = 0.1$ ps and $\tau = 1$ ps, respectively. All bond lengths of the solute were constrained using the LINCS algorithm [67] with an expansion order of 6, and the geometry of the water molecules was constrained using the SETTLE algorithm [68]. Electrostatic interactions were calculated using PME [69], with a real space cutoff of 10 Å and a Fourier spacing of 1.2 Å. For all production runs, a 4 fs integration was used, and the atom coordinates were saved every 100 ps, such that 10^5 snapshots were available for each trajectory. The trajectories for alanine dipeptide were taken from mdshare [70]. The structure for crambin was taken from PDB entry 1EJG [43].

Data Availability. All relevant data are available from the authors.

Code Availability. We have implemented our method in the Julia programming language [71]. The source code is available at <https://gitlab.gwdg.de/sschult/xfel>.

References

1. Hajdu, J. Single-Molecule X-ray Diffraction. *Current Opinion in Structural Biology* **10**, 569–573. ISSN: 0959-440X. <https://www.sciencedirect.com/science/article/pii/S0959440X00001330> (Oct. 1, 2000).
2. Huldt, G., Szőke, A. & Hajdu, J. Diffraction Imaging of Single Particles and Biomolecules. *Journal of Structural Biology. Analytical Methods and Software Tools for Macromolecular Microscopy* **144**, 219–227. ISSN: 1047-8477. <https://www.sciencedirect.com/science/article/pii/S1047847703001825> (Oct. 1, 2003).
3. Gaffney, K. J. & Chapman, H. N. Imaging Atomic Structure and Dynamics with Ultrafast X-ray Scattering. *Science* **316**, 1444–1448. ISSN: 0036-8075. pmid: 17556577. <https://www.science.org/doi/abs/10.1126/science.1135923> (2007).
4. Miao, J., Ishikawa, T., Robinson, I. K. & Murnane, M. M. Beyond Crystallography: Diffractive Imaging Using Coherent x-Ray Light Sources. *Science* **348**, 530–535. ISSN: 0036-8075. pmid: 25931551 (2015).

5. Chapman, H. N. *et al.* Femtosecond Diffractive Imaging with a Soft-X-ray Free-Electron Laser. *Nature Physics* **2**, 839–843. ISSN: 1745-2481. <https://www.nature.com/articles/nphys461> (12 Dec. 2006).
6. Chapman, H. N. *et al.* Femtosecond X-ray Protein Nanocrystallography. *Nature* **470**, 73–77. ISSN: 1476-4687. <https://www.nature.com/articles/nature09750> (7332 Feb. 2011).
7. Boutet, S. *et al.* High-Resolution Protein Structure Determination by Serial Femtosecond Crystallography. *Science*. <https://www.science.org/doi/abs/10.1126/science.1217737> (July 20, 2012).
8. Fromme, P. & Spence, J. C. Femtosecond Nanocrystallography Using X-ray Lasers for Membrane Protein Structure Determination. *Current Opinion in Structural Biology. Engineering and Design / Membranes* **21**, 509–516. ISSN: 0959-440X. <https://www.sciencedirect.com/science/article/pii/S0959440X11000947> (Aug. 1, 2011).
9. Kirian, R. A. *et al.* Femtosecond Protein Nanocrystallography—Data Analysis Methods. *Optics Express* **18**, 5713–5723. ISSN: 1094-4087. <https://www.osapublishing.org/oe/abstract.cfm?uri=oe-18-6-5713> (Mar. 15, 2010).
10. Schlichting, I. Serial Femtosecond Crystallography: The First Five Years. *IUCrJ* **2**, 246–255. ISSN: 2052-2525. [//scripts.iucr.org/cgi-bin/paper?it5004](https://scripts.iucr.org/cgi-bin/paper?it5004) (2 Mar. 1, 2015).
11. Roedig, P. *et al.* High-Speed Fixed-Target Serial Virus Crystallography. *Nature Methods* **14**, 805–810. ISSN: 1548-7105. <https://www.nature.com/articles/nmeth.4335> (8 Aug. 2017).
12. Barends, T. R. M., Stauch, B., Cherezov, V. & Schlichting, I. Serial Femtosecond Crystallography. *Nature Reviews Methods Primers* **2**, 1–24. ISSN: 2662-8449. <https://www.nature.com/articles/s43586-022-00141-7> (1 Aug. 4, 2022).
13. Ourmazd, A. Cryo-EM, XFELs and the Structure Conundrum in Structural Biology. *Nature Methods* **16**, 941–944. ISSN: 1548-7105. <https://www.nature.com/articles/s41592-019-0587-4> (10 Oct. 2019).
14. Van Thor, J. J. Advances and Opportunities in Ultrafast X-ray Crystallography and Ultrafast Structural Optical Crystallography of Nuclear and Electronic Protein Dynamics. *Structural Dynamics* **6**, 050901. <https://aca.scitation.org/doi/10.1063/1.5110685> (Sept. 2019).
15. Neutze, R., Wouts, R., van der Spoel, D., Weckert, E. & Hajdu, J. Potential for Biomolecular Imaging with Femtosecond X-ray Pulses. *Nature* **406**, 752–757. ISSN: 1476-4687. <https://www.nature.com/articles/35021099> (6797 Aug. 2000).
16. Seibert, M. M. *et al.* Single Mimivirus Particles Intercepted and Imaged with an X-ray Laser. *Nature* **470**, 78–81. ISSN: 1476-4687. <https://www.nature.com/articles/nature09748> (7332 Feb. 2011).
17. Ekeberg, T. *et al.* Three-Dimensional Reconstruction of the Giant Mimivirus Particle with an X-Ray Free-Electron Laser. *Physical Review Letters* **114**, 098102. <https://link.aps.org/doi/10.1103/PhysRevLett.114.098102> (Mar. 2, 2015).
18. Hosseinizadeh, A. *et al.* High-Resolution Structure of Viruses from Random Diffraction Snapshots. *Philosophical Transactions of the Royal Society B: Biological Sciences* **369**, 20130326. <https://royalsocietypublishing.org/doi/10.1098/rstb.2013.0326> (July 17, 2014).

19. Yoon, C. H. *et al.* A Comprehensive Simulation Framework for Imaging Single Particles and Biomolecules at the European X-ray Free-Electron Laser. *Scientific Reports* **6**, 24791. ISSN: 2045-2322. <https://www.nature.com/articles/srep24791> (1 Apr. 25, 2016).
20. Hantke, M. F., Ekeberg, T. & Maia, F. R. N. C. Condor: A Simulation Tool for Flash X-ray Imaging. *Journal of Applied Crystallography* **49**, 1356–1362. ISSN: 1600-5767. <http://scripts.iucr.org/cgi-bin/paper?zd5005> (4 Aug. 1, 2016).
21. Von Ardenne, B., Mechelke, M. & Grubmüller, H. Structure Determination from Single Molecule X-ray Scattering with Three Photons per Image. *Nature Communications* **9**, 2375. ISSN: 2041-1723. <https://www.nature.com/articles/s41467-018-04830-4> (1 June 18, 2018).
22. Shneerson, V. L., Ourmazd, A. & Saldin, D. K. Crystallography without Crystals. I. The Common-Line Method for Assembling a Three-Dimensional Diffraction Volume from Single-Particle Scattering. *Acta Crystallographica Section A: Foundations of Crystallography* **64**, 303–315. ISSN: 0108-7673. <http://scripts.iucr.org/cgi-bin/paper?mk5016> (2 Mar. 1, 2008).
23. Loh, N.-T. D. & Elser, V. Reconstruction Algorithm for Single-Particle Diffraction Imaging Experiments. *Physical Review E* **80**, 026705. <https://link.aps.org/doi/10.1103/PhysRevE.80.026705> (Aug. 24, 2009).
24. Walczak, M. & Grubmüller, H. Bayesian Orientation Estimate and Structure Information from Sparse Single-Molecule x-Ray Diffraction Images. *Physical Review E* **90**, 022714. <https://link.aps.org/doi/10.1103/PhysRevE.90.022714> (Aug. 20, 2014).
25. Kassemeyer, S. *et al.* Optimal Mapping of X-Ray Laser Diffraction Patterns into Three Dimensions Using Routing Algorithms. *Physical Review E* **88**, 042710. <https://link.aps.org/doi/10.1103/PhysRevE.88.042710> (Oct. 28, 2013).
26. Elser, V. Three-Dimensional Structure from Intensity Correlations. *New Journal of Physics* **13**, 123014. ISSN: 1367-2630. <https://doi.org/10.1088/1367-2630/13/12/123014> (Dec. 2011).
27. Tegze, M. & Bortel, G. Atomic Structure of a Single Large Biomolecule from Diffraction Patterns of Random Orientations. *Journal of Structural Biology* **179**, 41–45. ISSN: 1047-8477. <https://www.sciencedirect.com/science/article/pii/S1047847712001177> (July 1, 2012).
28. Donatelli, J. J., Sethian, J. A. & Zwart, P. H. Reconstruction from Limited Single-Particle Diffraction Data via Simultaneous Determination of State, Orientation, Intensity, and Phase. *Proceedings of the National Academy of Sciences* **114**, 7222–7227. ISSN: 0027-8424, 1091-6490. pmid: 28652365. <https://www.pnas.org/content/114/28/7222> (July 11, 2017).
29. Flamant, J., Le Bihan, N., Martin, A. V. & Manton, J. H. Expansion-Maximization-Compression Algorithm with Spherical Harmonics for Single Particle Imaging with x-Ray Lasers. *Physical Review E* **93**, 053302. <https://link.aps.org/doi/10.1103/PhysRevE.93.053302> (May 11, 2016).
30. Ayer, K., Lan, T.-Y., Elser, V. & Loh, N. D. Dragonfly: An Implementation of the Expand–Maximize–Compress Algorithm for Single-Particle Imaging. *Journal of Applied Crystallography* **49**, 1320–1335. ISSN: 1600-5767. <http://scripts.iucr.org/cgi-bin/paper?zf5002> (4 Aug. 1, 2016).

31. Fung, R., Shneerson, V., Saldin, D. K. & Ourmazd, A. Structure from Fleeting Illumination of Faint Spinning Objects in Flight. *Nature Physics* **5**, 64–67. ISSN: 1745-2481. <https://www.nature.com/articles/nphys1129> (1 Jan. 2009).
32. Moths, B. & Ourmazd, A. Bayesian Algorithms for Recovering Structure from Single-Particle Diffraction Snapshots of Unknown Orientation: A Comparison. *Acta Crystallographica Section A: Foundations of Crystallography* **67**, 481–486. ISSN: 0108-7673. <http://scripts.iucr.org/cgi-bin/paper?mk5026> (5 Sept. 1, 2011).
33. Schwander, P., Giannakis, D., Yoon, C. H. & Ourmazd, A. The Symmetries of Image Formation by Scattering. II. Applications. *Optics Express* **20**, 12827–12849. ISSN: 1094-4087. <https://www.osapublishing.org/oe/abstract.cfm?uri=oe-20-12-12827> (June 4, 2012).
34. Giannakis, D., Schwander, P. & Ourmazd, A. The Symmetries of Image Formation by Scattering. I. Theoretical Framework. *Optics Express* **20**, 12799–12826. ISSN: 1094-4087. <https://www.osapublishing.org/oe/abstract.cfm?uri=oe-20-12-12799> (June 4, 2012).
35. Saldin, D. K., Shneerson, V. L., Fung, R. & Ourmazd, A. Structure of Isolated Biomolecules Obtained from Ultrashort X-Ray Pulses: Exploiting the Symmetry of Random Orientations. *Journal of Physics: Condensed Matter* **21**, 134014. ISSN: 0953-8984. <https://doi.org/10.1088/0953-8984/21/13/134014> (Mar. 2009).
36. Saldin, D. K. *et al.* Beyond Small-Angle x-Ray Scattering: Exploiting Angular Correlations. *Physical Review B* **81**, 174105. <https://link.aps.org/doi/10.1103/PhysRevB.81.174105> (May 7, 2010).
37. Saldin, D. K. *et al.* New Light on Disordered Ensembles: Ab Initio Structure Determination of One Particle from Scattering Fluctuations of Many Copies. *Physical Review Letters* **106**, 115501. <https://link.aps.org/doi/10.1103/PhysRevLett.106.115501> (Mar. 14, 2011).
38. Saldin, D. K. *et al.* Structure of a Single Particle from Scattering by Many Particles Randomly Oriented about an Axis: Toward Structure Solution without Crystallization? *New Journal of Physics* **12**, 035014. ISSN: 1367-2630. <https://doi.org/10.1088/1367-2630/12/3/035014> (Mar. 2010).
39. Kurta, R. P. *et al.* Correlations in Scattered X-Ray Laser Pulses Reveal Nanoscale Structural Features of Viruses. *Physical Review Letters* **119**, 158102. <https://link.aps.org/doi/10.1103/PhysRevLett.119.158102> (Oct. 12, 2017).
40. Guaita, M., Watters, S. C. & Loerch, S. Recent Advances and Current Trends in Cryo-Electron Microscopy. *Current Opinion in Structural Biology* **77**, 102484. ISSN: 0959-440X. <https://www.sciencedirect.com/science/article/pii/S0959440X22001634> (Dec. 1, 2022).
41. Zhuang, Y. *et al.* Unsupervised Learning Approaches to Characterizing Heterogeneous Samples Using X-ray Single-Particle Imaging. *IUCrJ* **9**, 204–214. ISSN: 2052-2525. <https://journals.iucr.org/m/issues/2022/02/00/it5025/> (2 Mar. 1, 2022).
42. Hosseinizadeh, A. *et al.* Conformational Landscape of a Virus by Single-Particle X-ray Scattering. *Nature Methods* **14**, 877–881. ISSN: 1548-7105. pmid: 28805793 (Sept. 2017).
43. Jelsch, C. *et al.* Accurate Protein Crystallography at Ultra-High Resolution: Valence Electron Distribution in Crambin. *Proceedings of the National Academy of Sciences* **97**, 3171–3176. ISSN: 0027-8424, 1091-6490. pmid: 10737790. <https://www.pnas.org/content/97/7/3171> (Mar. 28, 2000).

44. Van Heel, M. & Schatz, M. Fourier Shell Correlation Threshold Criteria. *Journal of Structural Biology* **151**, 250–262. ISSN: 1047-8477. <https://www.sciencedirect.com/science/article/pii/S1047847705001292> (Sept. 1, 2005).
45. Scherer, M. K. *et al.* PyEMMA 2: A Software Package for Estimation, Validation, and Analysis of Markov Models. *Journal of Chemical Theory and Computation* **11**, 5525–5542. ISSN: 1549-9618. pmid: 26574340 (2015).
46. Ramachandran, G. N., Ramakrishnan, C. & Sasisekharan, V. Stereochemistry of Polypeptide Chain Configurations. *Journal of Molecular Biology* **7**, 95–99. ISSN: 0022-2836. pmid: 13990617 (July 1963).
47. Honda, S. *et al.* Crystal Structure of a Ten-Amino Acid Protein. *Journal of the American Chemical Society* **130**, 15327–15331. ISSN: 0002-7863. <https://doi.org/10.1021/ja8030533> (Nov. 19, 2008).
48. Zastra, U. *et al.* The High Energy Density Scientific Instrument at the European XFEL. *Journal of Synchrotron Radiation* **28**, 1393–1416. ISSN: 1600-5775. <https://journals.iucr.org/s/issues/2021/05/00/ay5578/> (Sept. 1, 2021).
49. Jumper, J. *et al.* Highly Accurate Protein Structure Prediction with AlphaFold. *Nature* **596**, 583–589. ISSN: 1476-4687. <https://www.nature.com/articles/s41586-021-03819-2> (7873 Aug. 2021).
50. Cossio, P. & Hummer, G. Bayesian Analysis of Individual Electron Microscopy Images: Towards Structures of Dynamic and Heterogeneous Biomolecular Assemblies. *Journal of Structural Biology* **184**, 427–437. ISSN: 1047-8477. <https://www.sciencedirect.com/science/article/pii/S1047847713002712> (Dec. 1, 2013).
51. Grant, T., Rohou, A. & Grigorieff, N. cisTEM, User-Friendly Software for Single-Particle Image Processing. *eLife* **7** (ed Egelman, E. H.) e35383. ISSN: 2050-084X. <https://doi.org/10.7554/eLife.35383> (Mar. 7, 2018).
52. Punjani, A., Rubinstein, J. L., Fleet, D. J. & Brubaker, M. A. cryoSPARC: Algorithms for Rapid Unsupervised Cryo-EM Structure Determination. *Nature Methods* **14**, 290–296. ISSN: 1548-7105. <https://www.nature.com/articles/nmeth.4169> (3 Mar. 2017).
53. Lyumkis, D., Brilot, A. F., Theobald, D. L. & Grigorieff, N. Likelihood-Based Classification of Cryo-EM Images Using FREALIGN. *Journal of Structural Biology* **183**, 377–388. ISSN: 1047-8477. <https://www.sciencedirect.com/science/article/pii/S1047847713001858> (Sept. 1, 2013).
54. Scheres, S. H. W. in *Methods in Enzymology* (ed Crowther, R. A.) 125–157 (Academic Press, Jan. 1, 2016). <https://www.sciencedirect.com/science/article/pii/S0076687916300301>.
55. Tang, G. *et al.* EMAN2: An Extensible Image Processing Suite for Electron Microscopy. *Journal of Structural Biology. Software Tools for Macromolecular Microscopy* **157**, 38–46. ISSN: 1047-8477. <https://www.sciencedirect.com/science/article/pii/S1047847706001894> (Jan. 1, 2007).
56. Zivanov, J. *et al.* New Tools for Automated High-Resolution Cryo-EM Structure Determination in RELION-3. *eLife* **7** (eds Egelman, E. H. & Kuriyan, J.) e42166. ISSN: 2050-084X. <https://doi.org/10.7554/eLife.42166> (Nov. 9, 2018).

57. Kinman, L. F., Powell, B. M., Zhong, E. D., Berger, B. & Davis, J. H. Uncovering Structural Ensembles from Single-Particle Cryo-EM Data Using cryoDRGN. *Nature Protocols*, 1–31. ISSN: 1750-2799. <https://www.nature.com/articles/s41596-022-00763-x> (Nov. 14, 2022).
58. *SPHERE_LEBEDEV_RULE - Quadrature Rules for the Sphere* https://people.sc.fsu.edu/~jburkardt/datasets/sphere_lebedev_rule/sphere_lebedev_rule.html.
59. Gräf, M. & Potts, D. Sampling Sets and Quadrature Formulae on the Rotation Group. *Numerical Functional Analysis and Optimization* **30**, 665–688. ISSN: 0163-0563 (2009).
60. Abraham, M. J. *et al.* GROMACS: High Performance Molecular Simulations through Multi-Level Parallelism from Laptops to Supercomputers. *SoftwareX* **1–2**, 19–25. ISSN: 2352-7110. <https://www.sciencedirect.com/science/article/pii/S2352711015000059> (Sept. 1, 2015).
61. Huang, J. *et al.* CHARMM36m: An Improved Force Field for Folded and Intrinsically Disordered Proteins. *Nature Methods* **14**, 71–73. ISSN: 1548-7105. <https://www.nature.com/articles/nmeth.4067> (1 Jan. 2017).
62. Izadi, S., Anandakrishnan, R. & Onufriev, A. V. Building Water Models: A Different Approach. *The Journal of Physical Chemistry Letters* **5**, 3863–3871. ISSN: 1948-7185. pmid: 25400877. <https://www.ncbi.nlm.nih.gov/pmc/articles/PMC4226301/> (Nov. 6, 2014).
63. Berman, H. M. *et al.* The Protein Data Bank. *Nucleic Acids Research* **28**, 235–242. ISSN: 0305-1048. pmid: 10592235 (Jan. 1, 2000).
64. Feenstra, K. A., Hess, B. & Berendsen, H. J. C. Improving Efficiency of Large Time-Scale Molecular Dynamics Simulations of Hydrogen-Rich Systems. *Journal of Computational Chemistry* **20**, 786–798. ISSN: 1096-987X. <https://onlinelibrary.wiley.com/doi/abs/10.1002/%28SICI%291096-987X%28199906%2920%3A8%3C786%3A%3AAID-JCC5%3E3.0.CO%3B2-B> (1999).
65. Bussi, G., Donadio, D. & Parrinello, M. Canonical Sampling through Velocity Rescaling. *The Journal of Chemical Physics* **126**, 014101. ISSN: 0021-9606. <https://aip.scitation.org/doi/10.1063/1.2408420> (Jan. 3, 2007).
66. Parrinello, M. & Rahman, A. Polymorphic Transitions in Single Crystals: A New Molecular Dynamics Method. *Journal of Applied Physics* **52**, 7182–7190. ISSN: 0021-8979. <https://aip.scitation.org/doi/10.1063/1.328693> (Dec. 1, 1981).
67. Hess, B., Bekker, H., Berendsen, H. J. C. & Fraaije, J. G. E. M. LINCS: A Linear Constraint Solver for Molecular Simulations. *Journal of Computational Chemistry* **18**, 1463–1472. ISSN: 1096-987X. <https://onlinelibrary.wiley.com/doi/abs/10.1002/%28SICI%291096-987X%28199709%2918%3A12%3C1463%3A%3AAID-JCC4%3E3.0.CO%3B2-H> (1997).
68. Miyamoto, S. & Kollman, P. A. Settle: An Analytical Version of the SHAKE and RATTLE Algorithm for Rigid Water Models. *Journal of Computational Chemistry* **13**, 952–962. ISSN: 1096-987X. <https://onlinelibrary.wiley.com/doi/abs/10.1002/jcc.540130805> (1992).
69. Darden, T., York, D. & Pedersen, L. Particle Mesh Ewald: An N·log(N) Method for Ewald Sums in Large Systems. *The Journal of Chemical Physics* **98**, 10089–10092. ISSN: 0021-9606. <https://aip.scitation.org/doi/10.1063/1.464397> (June 15, 1993).
70. *Mdshare* mdshare. <https://markovmodel.github.io/mdshare/>.

71. Bezanson, J., Edelman, A., Karpinski, S. & Shah, V. B. Julia: A Fresh Approach to Numerical Computing. *SIAM Review* **59**, 65–98. ISSN: 0036-1445. <https://epubs.siam.org/doi/10.1137/141000671> (Jan. 2017).
72. Behboodian, J. Information Matrix for a Mixture of Two Normal Distributions. *Journal of Statistical Computation and Simulation* **1**, 295–314. ISSN: 0094-9655. <https://doi.org/10.1080/00949657208810024> (Oct. 1, 1972).
73. Gelman, A., Gilks, W. R. & Roberts, G. O. Weak Convergence and Optimal Scaling of Random Walk Metropolis Algorithms. *The Annals of Applied Probability* **7**, 110–120. ISSN: 1050-5164, 2168-8737. <https://projecteuclid.org/journals/annals-of-applied-probability/volume-7/issue-1/Weak-convergence-and-optimal-scaling-of-random-walk-Metropolis-algorithms/10.1214/aoap/1034625254.full> (Feb. 1997).

Acknowledgments

This work was financially supported by the Federal Ministry of Education and Research through the joint research project 05K20EGA Fluctuation XFEL, and the Deutsche Forschungsgemeinschaft (DFG, German Research Foundation) - CRC 1456/1 - 432680300. The MD-trajectories were kindly provided by Nicolai Kozlowski.

Author contributions

S.S. and H.G. conceived research, S.S. carried out research, S.S. and H.G. wrote paper.

Competing interests

The authors declare no competing interests.

Appendices

1 Parameters

The parameters used for the test cases are shown in Table 1. The Lebedev precision and the number of angular rotations S_j are chosen such that the expected angular distance between nearest neighbors in the resulting grid is smaller than the length scale corresponding to the desired relative resolution divided by the approximate radius of the molecule. Due to hardware constraints, the number of angular rotations must be a multiple of 32. The parameters for image selection (r_i and m_i) were chosen such that the radial distribution of photons in the selected images was close to uniform up to the desired resolution level.

| Name | Stage | total images | selected images | n_i | r_i [1/Å] | σ [Å] | $t_{1/2}$ | m | n | Lebedev precision | angular rotations |
|-----------|-------|-------------------|-----------------|-----------|------------------------------|--------------|----------------|-----|-----|-------------------|-------------------|
| Crambin | 1 | $8.96 \cdot 10^3$ | 1,000 | (4) | (0.25, ∞) | 2.0 | $1 \cdot 10^3$ | 12 | 1 | 23 | 32 |
| | 2 | $1.00 \cdot 10^7$ | 19,315 | (3, 2) | (0.33, 0.5, ∞) | 1.5 | $1 \cdot 10^4$ | 23 | 1 | 47 | 32 |
| | 3 | $3.04 \cdot 10^6$ | 50,000 | (1, 1, 2) | (0.35, 0.5, 0.65, ∞) | 1.2 | $2 \cdot 10^4$ | 46 | 1 | 47 | 64 |
| | 4 | $1.00 \cdot 10^8$ | 204,447 | (1, 2, 2) | (0.35, 0.5, 0.8, ∞) | 0.9 | $1 \cdot 10^5$ | 92 | 1 | 89 | 64 |
| | 5 | $1.00 \cdot 10^8$ | 634,032 | (1, 1, 3) | (0.4, 0.65, 0.9, ∞) | 0.5 | $1 \cdot 10^5$ | 184 | 1 | 89 | 64 |
| Dipeptide | 1 | $1.00 \cdot 10^6$ | 3,965 | (4, 4) | (0.9, 1.3, ∞) | 0.5 | $1 \cdot 10^3$ | 10 | 2 | 23 | 32 |
| | 2 | $1.00 \cdot 10^6$ | - | - | - | 0.0 | $5 \cdot 10^3$ | 10 | 8 | 35 | 32 |
| Chignolin | 1 | $1.00 \cdot 10^4$ | - | - | - | 2.5 | $1 \cdot 10^3$ | 5 | 2 | 23 | 32 |
| | 2 | $1.09 \cdot 10^7$ | 100,000 | (2, 2) | (0.4, 0.6, ∞) | 1.5 | $5 \cdot 10^3$ | 10 | 4 | 23 | 32 |
| | 3 | $1.24 \cdot 10^7$ | 100,000 | (2, 3) | (0.4, 0.6, ∞) | 1.2 | $1 \cdot 10^4$ | 20 | 6 | 47 | 64 |

Table 1: Parameters for the three test cases.

2 Expected information content of scattering images

The information content of scattering image on structural ensembles can be estimated analogous to an argument for mixtures of normal distributions [72], as follows. Consider an ensemble of two structures ρ_1 and ρ_2 with weights w and $1 - w$, respectively. The probability of observing an image x is then a mixture of the two single distributions,

$$p(x; \rho_1, \rho_2) = wp(x; \rho_1) + (1 - w)p(x; \rho_2). \quad (7)$$

By the Bayesian central limit theorem, in the limit of many scattering images the posterior becomes a multivariate normal distribution with covariance $N^{-1}I^{-1}$,

$$P(\rho_1, \rho_2 | \mathcal{I}) \approx \mathcal{N}(\rho_1, \rho_2; N^{-1}I^{-1}), \quad (8)$$

where N is the number of images, and I the Fisher information matrix. The first diagonal element of this matrix is approximately proportional to the weight squared,

$$I_{\rho_1 \rho_1} = \mathbb{E} \left[\left(\frac{\partial}{\partial \rho_1} \log p(x; \rho_1, \rho_2) \right)^2 \right] = \mathbb{E} \left[\left(\frac{w \frac{\partial}{\partial \rho_1} p(x; \rho_1)}{p(x; \rho_1, \rho_2)} \right)^2 \right] = w^2 \mathbb{E} \left[\left(\frac{\frac{\partial}{\partial \rho_1} p(x; \rho_1)}{p(x; \rho_1, \rho_2)} \right)^2 \right]. \quad (9)$$

Therefore, under the assumption that the off-diagonal elements are small, the limiting variance for ρ_1 becomes $1/(Nw^2)$. An similar argument can be carried out for more than two distinct structures. In the special case of uniform weights $w = 1/n$ the limiting variance becomes n^2/N , consistent with the quadratic scaling observed in Fig. 5.

3 Computation

The integral over $\text{SO}(3)$ is approximated by a finite sum over rotations \mathbf{R}_i with weights s_i ,

$$P(\mathbf{k}_1, \dots, \mathbf{k}_n | \rho) \approx \frac{N^n}{n!} \sum_i s_i \exp \left(-N \int_D I(\mathbf{R}_i \mathbf{k}) d\mathbf{k} \right) \prod_{j=1}^n I(\mathbf{R}_i \mathbf{k}_j) \quad (10)$$

Computing this sum involves evaluating the intensity function I at all points of the form $\mathbf{R}_i \mathbf{k}_j$. Since this has to be done for all the images, this leads to a very large number of evaluations of I . It is therefore efficient to first discretize the images. To that end, the detector is pixelated, that is, partitioned into a grid of cells with centers \mathbf{x}_k and areas a_k . Each image $\mathbf{k}_1, \dots, \mathbf{k}_n$ is replaced with a set of indices k_1, \dots, k_n , such that for each \mathbf{k}_i the closest point in the grid is \mathbf{x}_{k_i} . In this setting, the probability distribution becomes

$$P(k_1, \dots, k_n | \rho) \approx \frac{N^n}{n!} \sum_i s_i \exp \left(-N \sum_k a_k I(\mathbf{R}_i \mathbf{x}_k) \right) \prod_{j=1}^n a_{k_j} I(\mathbf{R}_i \mathbf{x}_{k_j}) \quad (11)$$

To construct the quadrature rule for $\text{SO}(3)$, we proceed as follows. First, we choose a Lebedev grid as a uniform grid of points \mathbf{v}_i in the 2-sphere S^2 . For each one of these, we find a rotation $Q_i \in \text{SO}(3)$ such that $Q_i \mathbf{v}_i \parallel \mathbf{k}_0$. In addition, let S_j be uniformly spaced rotations around the axis defined by \mathbf{k}_0 . The set of products $S_j Q_i$ is then a uniform grid in $\text{SO}(3)$. Equation (11) becomes

$$P(k_1, \dots, k_n | \rho) \approx \frac{N^n}{n!} \sum_{i,j} s_i \exp \left(-N \sum_k a_k I(Q_i S_j \mathbf{x}_k) \right) \prod_{m=1}^n a_{k_m} I(Q_i S_j \mathbf{x}_{k_m}) \quad (12)$$

Choosing the pixel grid \mathbf{x}_k such that it is rotationally symmetric allows further simplification. We reindex it as $\mathbf{x}_{k,l}$, such that $S_j \mathbf{x}_{k,l} = \mathbf{x}_{k+j,l}$. Here, the first index is considered cyclic, that is, if, say, k ranges from 1 to k_{\max} , then $\mathbf{x}_{k+j,l}$ is to be interpreted as $\mathbf{x}_{(k+j \bmod k_{\max}),l}$. The corresponding areas $a_{k,l}$ only depend on l , so we write $a_l = a_{k,l}$. The images now also consist of these new indices. Plugging this in, we get

$$P(k_1, l_1, \dots, k_n, l_n | \rho) \approx \frac{N^n}{n!} \sum_{i,j} w_i \exp \left(-N \sum_{k,l} a_l I(Q_i S_j \mathbf{x}_{k,l}) \right) \prod_{m=1}^n a_{l_m} I(Q_i S_j \mathbf{x}_{k_m, l_m}) \quad (13)$$

$$= \frac{N^n}{n!} \sum_i w_i \exp \left(-N \sum_{k,l} a_l I(Q_i \mathbf{x}_{k,l}) \right) \sum_j \prod_{m=1}^n a_{l_m} I(Q_i \mathbf{x}_{k_m+j, l_m}) \quad (14)$$

$$= \frac{N^n}{n!} \sum_i w_i P_i \sum_j \prod_{m=1}^n I_{i, k_m+j, l_m} \quad (15)$$

The values $I_{i,k,l} := a_l I(Q_i \mathbf{x}_{k,l})$ and $P_i := \exp(-N \sum_{k,l} I_{i,k,l})$ can be computed in advance and reused for each image.

Due to limited floating point precision, a number of adjustments must be made. Due to the large value of N , computing P_i results in underflow. Therefore, we write

$$\tilde{P}_i = P_i / \bar{P}, \quad \bar{P} = \left(\prod_{i'=1}^{i_{\max}} P_{i'} \right)^{\frac{1}{i_{\max}}}. \quad (16)$$

Further, $I_{i,k,l} \ll 1$, so if the images contain enough photons the product over m will underflow. Since the magnitude of $I_{i,k,l}$ depends mostly on l , we define

$$\tilde{I}_{i,k,l} = I_{i,k,l} / \bar{I}_l, \quad \bar{I}_l = \frac{1}{i_{\max} k_{\max}} \sum_{i'=1}^{i_{\max}} \sum_{k'=1}^{k_{\max}} I_{i',k',l} \quad (17)$$

Both \bar{P} and \bar{I}_l do not depend on the rotation index i and factor out,

$$P(k_1, l_1, \dots, k_n, l_n | \rho) \approx \frac{N^n}{n!} \bar{P} \left(\prod_{m=1}^n \bar{I}_{l_m} \right) \sum_i w_i \tilde{P}_i \sum_j \prod_{m=1}^n \tilde{I}_{i, k_m + j, l_m} \quad (18)$$

Taking the logarithm,

$$\log P(k_1, l_1, \dots, k_n, l_n | \rho) \approx \log \frac{N^n}{n!} + \log \bar{P} + \sum_{m=1}^n \log \bar{I}_{l_m} + \log \sum_i w_i \tilde{P}_i \sum_j \prod_{m=1}^n \tilde{I}_{i, k_m + j, l_m}, \quad (19)$$

we see that only $\log \bar{P}$ and $\log \bar{I}_l$ appear, which can be computed without overflow.

4 Monte Carlo Simulated Annealing

Let $\boldsymbol{\rho} = (\rho_1, \dots, \rho_n)$ and $\mathbf{w} = (w_1, \dots, w_n)$ denote vectors of electron densities and weights, respectively. A Markov chain of structural ensembles $\boldsymbol{\rho}_t$ with weights \mathbf{w}_t was constructed iteratively using a Metropolis-within-Gibbs algorithm. This algorithm works as follows. For each step t , first a Metropolis step for the structures is performed, that is, new candidate structures $\boldsymbol{\rho}'$ are drawn from a proposal distribution $g(\boldsymbol{\rho}' | \boldsymbol{\rho}_t)$, and this candidate is accepted ($\boldsymbol{\rho}_{t+1} = \boldsymbol{\rho}'$) or rejected ($\boldsymbol{\rho}_{t+1} = \boldsymbol{\rho}_t$) with probability

$$1 \wedge \exp \left(\frac{\log P(\boldsymbol{\rho}', \mathbf{w}_t | \mathcal{I}) - \log P(\boldsymbol{\rho}_t, \mathbf{w}_t | \mathcal{I}) + \log g(\boldsymbol{\rho}_t | \boldsymbol{\rho}') - \log g(\boldsymbol{\rho}' | \boldsymbol{\rho}_t)}{T(t)} \right), \quad (20)$$

adopting the notation $1 \wedge x = \min(1, x)$. The temperature $T(t)$ is determined according to an exponential annealing schedule $T(t) = T_0 \exp(-\lambda t)$ for some constant λ . The proposal density g is an isotropic normal distribution $\mathcal{N}(\boldsymbol{\rho}_t, d)$ around $\boldsymbol{\rho}_t$, that is, to obtain the candidate, the position of each Gaussian in the structure representation is perturbed by a normally distributed amount; or it is given by our hierarchical sampling method as described in the next section. The step size d is determined iteratively such that the acceptance rate is the optimal 23% [73], by increasing or decreasing it after a successful or unsuccessful step, respectively.

Second, a separate Metropolis step for the weights is performed. To correctly sample from the n -simplex of weights w_i such that $w_i \leq 0$ and $\sum_i w_i = 1$, we introduce variables $s_j \leq 0$ such that $w_i = s_i / \sum_j s_j$. For these variables, the proposals are drawn from a Gamma distribution of mean s_j and standard deviation given by the current step size. Note that this is not a proposal distribution in the sense of equation (20), as it does not appear in the acceptance probability. If one of the weights w_i becomes zero during the sampling process, the corresponding structure ρ_i does no longer affect the posterior probability, hindering convergence. To prevent this, a delayed acceptance scheme is used as follows. Each proposal \mathbf{s}' with corresponding weights \mathbf{w}' generated by the above procedure is accepted with probability

$$g^*(\mathbf{w}' | \mathbf{w}_t) = 1 \wedge \exp \left(\frac{1}{2\nu} \|\mathbf{w}' - \mathbf{c}\|^2 - \frac{1}{2\nu} \|\mathbf{w}_t - \mathbf{c}\|^2 \right), \quad (21)$$

where $\mathbf{c} = (1/n, \dots, 1/n)$ and ν is sufficiently small to ensure that the weights remain non-zero. Finally, the proposal is accepted with probability

$$1 \wedge \exp \left(\frac{\log P(\boldsymbol{\rho}_{t+1}, \mathbf{w}' | \mathcal{I}) - \log P(\boldsymbol{\rho}_{t+1}, \mathbf{w}_t | \mathcal{I}) + \log g^*(\mathbf{w}_t | \mathbf{w}') - \log g^*(\mathbf{w}' | \mathbf{w}_t)}{T(t)} \right). \quad (22)$$

The metropolis step for the weights has little computational cost, as the computationally costly parts of equation (3) are unaffected. Therefore, it is repeated multiple times in each iteration.

5 Proposal density for hierarchical sampling

In each hierarchical sampling stage, the number of Gaussian functions was doubled, and the reduced resolution structure determined by the previous stage was used as a proposal density to improve convergence in the simulated annealing, as follows. Let $\mathbf{y}_1, \dots, \mathbf{y}_n$ be the positions of the Gaussian functions from the previous stage, and $\mathbf{z}_1, \dots, \mathbf{z}_{2n}$ those of the current stage. Then the proposal density was, up to normalization, given by

$$g(\mathbf{z}'_1, \dots, \mathbf{z}'_{2n} | \mathbf{z}_1, \dots, \mathbf{z}_{2n}) \propto \prod_{i=1}^{2n} \exp\left(-\frac{\|\mathbf{z}'_i - \mathbf{z}_i\|^2}{2\sigma^2}\right) \prod_{i=1}^n \exp\left(-\frac{\|\mathbf{z}'_{2i} - \mathbf{y}_i\|^2 + \|\mathbf{y}'_{2i+1} - \mathbf{y}_i\|^2}{2w^2}\right), \quad (23)$$

where w is the width of the Gaussians from the previous stage. For ensembles of structures, the proposal density becomes a product over the single structures ρ_i with separate intermediates for each ρ_i ,

$$g(\rho' | \rho_t) = \prod_{i=1}^n g(\rho'_i | \rho_i), \quad (24)$$

where $g(\rho'_i | \rho_i)$ is the proposal density from equation (23).

6 Image selection

In our hierarchical sampling scheme, images containing only photons with $|\mathbf{k}|$ below a threshold are no longer useful, and the computations were sped up by removing these images. To achieve this, numbers (r_i) and integers m_i were chosen, and only the subset \mathcal{I}_C of those images was used that fulfilled the condition $C(I)$ that for each i the image I contains at least m_i photons with $r_i < |\mathbf{k}| < r_{i+1}$. To ensure that the posterior was not biased by this filtering, it was taken into account in the Bayesian formalism by dividing by the probability $P(C | \rho, \mathbf{w})$ that an image fulfills C . In other words, the original posterior probability was replaced with $P(\rho, \mathbf{w} | \mathcal{I}_C, C) \propto P(\mathcal{I}_C | \rho, \mathbf{w}) / P(C | \rho, \mathbf{w})$. The probability that an image fulfills C depends on both the orientation \mathbf{R} and the conformer i . Therefore, $P(C | \rho, \mathbf{w})$ was obtained by averaging over both,

$$P(C | \rho, \mathbf{w}) = \sum_j w_j \int_{\text{SO}(3)} \prod_i \left(1 - Q\left(m_i - 1, N \int_{D_i} |F\{\rho_j\}(\mathbf{R}\mathbf{k})|^2 d\mathbf{k}\right)\right) d\mathbf{R}, \quad (25)$$

where $Q(x, \lambda)$ is the cumulative distribution function of a Poisson distribution with mean λ and $D_i = \{\mathbf{k} \in D | r_i < \|\mathbf{k}\| < r_{i+1}\}$ is the relevant slice of the Ewald sphere.